Please cite this article in press as: Lacoste et al., Sensory-Related Neural Activity Regulates the Structure of Vascular Networks in the Cerebral Cortex, Neuron (2014), http://dx.doi.org/10.1016/j.neuron.2014.07.034

Neuron
Article

Sensory-Related Neural Activity Regulates the Structure of Vascular Networks in the Cerebral Cortex

Baptiste Lacoste,[1] Cesar H. Comin,[2] Ayal Ben-Zvi,[1] Pascal S. Kaeser,[1] Xiaoyin Xu,[3] Luciano da F. Costa,[2] and Chenghua Gu[1,*]
[1]Department of Neurobiology, Harvard Medical School, Boston, MA, USA
[2]IFSC, University of Sao Paulo, Sao Carlos, SP, Brazil
[3]Department of Radiology, Brigham and Women's Hospital, Boston, MA, USA
*Correspondence: chenghua_gu@hms.harvard.edu
http://dx.doi.org/10.1016/j.neuron.2014.07.034

SUMMARY

Neurovascular interactions are essential for proper brain function. While the effect of neural activity on cerebral blood flow has been extensively studied, whether or not neural activity influences vascular patterning remains elusive. Here, we demonstrate that neural activity promotes the formation of vascular networks in the early postnatal mouse barrel cortex. Using a combination of genetics, imaging, and computational tools to allow simultaneous analysis of neuronal and vascular components, we found that vascular density and branching were decreased in the barrel cortex when sensory input was reduced by either a complete deafferentation, a genetic impairment of neurotransmitter release at thalamocortical synapses, or a selective reduction of sensory-related neural activity by whisker plucking. In contrast, enhancement of neural activity by whisker stimulation led to an increase in vascular density and branching. The finding that neural activity is necessary and sufficient to trigger alterations of vascular networks reveals an important feature of neurovascular interactions.

INTRODUCTION

Proper function of precisely wired neural circuits depends on a close physical and functional relationship with a complex and overlapping network of blood vessels (Lecrux and Hamel, 2011; Zlokovic, 2010). The brain is more dependent than any other organ on a continuous supply of oxygen and nutrients from blood vessels, and high metabolic activity correlates with higher vascular density (Riddle et al., 1993). Nerves, in turn, control blood vessel dilation and contraction, as well as heart rate. To date, neurovascular interactions are best known for their functional matching in hemodynamics, where increased neural activity leads to increased blood flow (Drake and Iadecola, 2007; Hamel, 2006). However, whether neuronal function and/or neuronal cytoarchitecture have any impact on vascular network structure remains elusive.

Vascular patterning is critical for the proper function of the brain, given its high metabolic demand and vulnerability to ischemia. During early embryonic development, common guidance cues and receptors are responsible for the basic hard wiring of both networks (Carmeliet and Tessier-Lavigne, 2005; Gelfand et al., 2009), and it is well known that after birth neural activity continues to fine-tune neural connectivity (Fu and Zuo, 2011; Katz and Shatz, 1996). Similar microvascular remodeling continues into early postnatal stages. However, compared to the wealth of literature on neural plasticity, knowledge about vascular plasticity is still very limited. The concept of activity-induced vascular plasticity was first introduced only 20 years ago by reports in rats correlating angiogenesis to sensorimotor experience (Black et al., 1987, 1990). Since then, very few additional studies have investigated vascular plasticity due to the lack of proper tools to simultaneously visualize the 3D structure of both neuronal and vascular modules with high resolution, and it has been controversial whether natural/endogenous neural activity has any impact on vascular patterning (Whiteus et al., 2014).

To address whether neural activity influences vascular structure in the brain, we developed an integrative approach combining mouse genetics, high-resolution 3D imaging, and computational image analysis. We chose the mouse barrel cortex as a model system, where thalamocortical axons (TCAs) organize in a somatotopic sensory map in which one whisker is represented by one barrel (Woolsey, 1978). In this brain region, the neuronal cytoarchitecture is subject to a high degree of plasticity during a critical time window, and neural activity can easily be manipulated through the whisker pathway (Harris and Woolsey, 1981; Kleinfeld and Deschênes, 2011; McCasland and Woolsey, 1988; Woolsey and Wann, 1976). This system thus provides a suitable model to test the role of sensory inputs in shaping vascular networks.

We demonstrate that manipulations of sensory inputs result in vascular structural changes, such that local sensory-related neural activity promotes the formation of cerebrovascular networks. Four different paradigms in which large-scale neuronal cytoarchitecture and neural activity are differentially affected in layer IV were performed: (1) whisker lesions, where both neuronal cytoarchitecture and neural activity are abolished; (2) genetic reduction of thalamocortical neurotransmission where the postsynaptic neuronal cytoarchitecture is

abolished and neural activity is reduced; (3) whisker plucking, which selectively reduces neural activity while maintaining the neuronal cytoarchitecture; and (4) whisker stimulation leading to enhancement of neural activity only. Sensory deprivation and stimulation resulted in opposing effects on the vascular structure, even in absence of neuroarchitectural changes, indicating that neural activity is necessary for vascular patterning and that changes in neural activity are sufficient to affect vascular structure. Moreover, neuroarchitectural changes did not produce additional vascular alterations, further demonstrating the significant role of neural activity in regulating the structure of cerebrovascular networks. These findings definitively link neural activity to vascular network formation and therefore reveal a crucial aspect of neurovascular interactions.

RESULTS

A Combination of Genetics, Imaging, and Computational Tools to Study Neurovascular Development and Plasticity in the Mouse Cerebral Cortex

To selectively and simultaneously analyze vascular and neuronal components in layer IV of the barrel cortex, we constructed a compound transgenic mouse in which TCAs are genetically labeled by tdTomato (tdT) expression under the serotonin transporter (Sert) promoter (*Sert-Cre:tdT$^{flox\text{-}stop\text{-}flox}$*) and in which blood vessels are labeled through GFP expression under the endothelial-specific Tie2 promoter (*Tie2-GFP*) (Figures 1A and 1B; Figure S1A and S1B available online). With additional immunostaining for neuronal nuclei (NeuN) revealing cortical neurons that are densely packed and form barrel septa delimiting barrel hollows (TCAs), the neuronal cytoarchitecture of barrel cortex layer IV and its underlying vascular bed are easily visualized simultaneously with high resolution. As the brain microvasculature develops and elaborates, its complex 3D structure makes it challenging to detect and quantify fine-scale changes in vascular networks. To overcome this hurdle, we implemented a computational tool that unbiasedly processes 3D confocal images and automatically quantifies parameters of vascular morphology, including vessel density, vessel diameter, and branching patterns (Figures 1C and S1C; see Experimental Procedures for details). Moreover, immunostaining with anti-GFP greatly improved the detection of the microvascular bed (Figure S1D). Using this approach, we demonstrate that in layer IV of the barrel cortex, vascular density and branching progressively increase after birth and reach a peak at postnatal day 14 (P14) (Figure 1D). Then, from P14 to P30, vascular density and branching decrease (Figure 1D). The values obtained with our image analysis, including vessel density and diameter, are in line with recent studies in the mouse cerebral cortex (Ben-Zvi et al., 2014; Blinder et al., 2013; Harb et al., 2013). The combination of these tools allowed us to ask the fundamental question of whether changes in neuronal cytoarchitecture and/or neural activity lead to structural changes of the brain vasculature.

Developmental Profile of Neuronal and Vascular Organization in Barrel Cortex Layer IV

We first examined neurovascular modules in layer IV of the barrel cortex during an early postnatal stage when neural plasticity is in a critical period. At birth (P0), TCAs are only starting to invade the cortex, and a rudimentary vasculature is already present in the cortical area where future barrels will form (Figure 2). Between P3 and P5, the vasculature continues to expand while barrel septa (cortical neurons) begin to organize and barrel hollows (TCAs) are hardly noticeable. At P7, barrel hollows and septa become clear, and the vasculature has further expanded (Figure 2).

A Complete Deafferentation by Whisker Follicle Lesions Abolishes the Neuroarchitecture and Results in a Reduction of Vascular Density and Branching in Layer IV of the Barrel Cortex

Since during a critical developmental window (P0 to P5) neuronal circuits undergo massive alteration when neural activity is suppressed (Erzurumlu and Gaspar, 2012; Harris and Woolsey, 1981; Woolsey and Wann, 1976), we hypothesize that neuronal cytoarchitecture and/or neural activity may contribute to the expansion of vascular networks during early life. To test this hypothesis, we first examined the impact of a complete deafferentation on the vasculature in barrel cortex layer IV. When the central row (row c) of whisker follicles is unilaterally lesioned at birth, formation of its cortical representation is impaired, appearing shrunken at P14, with absence of axonal and neuronal patterning and expansion of surrounding rows (Figures 3A–3D, S2A, and S2B). Importantly, analysis of vascular images (Figures S2C and S2D) revealed a significant reduction of vascular density and branching in layer IV within the contralateral row c compared to the ipsilateral (control) row c (Figures 3D and 3E). In that volume, the total neuronal density (Figure 3B) and the local neuronal density around vessels (Figure 3C) remained unchanged.

We then tested whether inflicting a wider lesion by cauterizing three central whisker rows (b, c, and d) could lead to more devastating changes in vascular structure. In this condition, the layer IV neuronal cytoarchitecture appears severely altered in the deafferented row c "ghost" volume (Figure 3D). The microvascular bed within that volume also displayed reduced vascular density and branching (Figure 3F); however, no additional reduction (percentage of decrease) in these parameters was evidenced compared to a single row lesion ($p > 0.05$, unpaired t test) (Figures 3E and 3F). Together, these results demonstrate that neuronal cytoarchitecture and/or neural activity promote local formation of vascular networks during the critical period of neural plasticity.

Genetic Reduction of Neurotransmitter Release at Thalamocortical Synapses Impairs Postsynaptic Neuroarchitecture and Leads to a Reduction of Vascular Density and Branching in Layer IV of the Barrel Cortex

We next sought to dissect the individual contribution of neuronal cytoarchitecture (TCAs and cortical neurons) versus sensory-related neural activity to vascular plasticity. Presynaptic Rab3-interacting molecules (RIMs) are active zone molecules involved in the control of neurotransmitter release (Kaeser et al., 2011; Wang et al., 1997). Previous work demonstrated that postsynaptic layer IV barrels do not form when neurotransmission is reduced selectively at thalamocortical synapses following

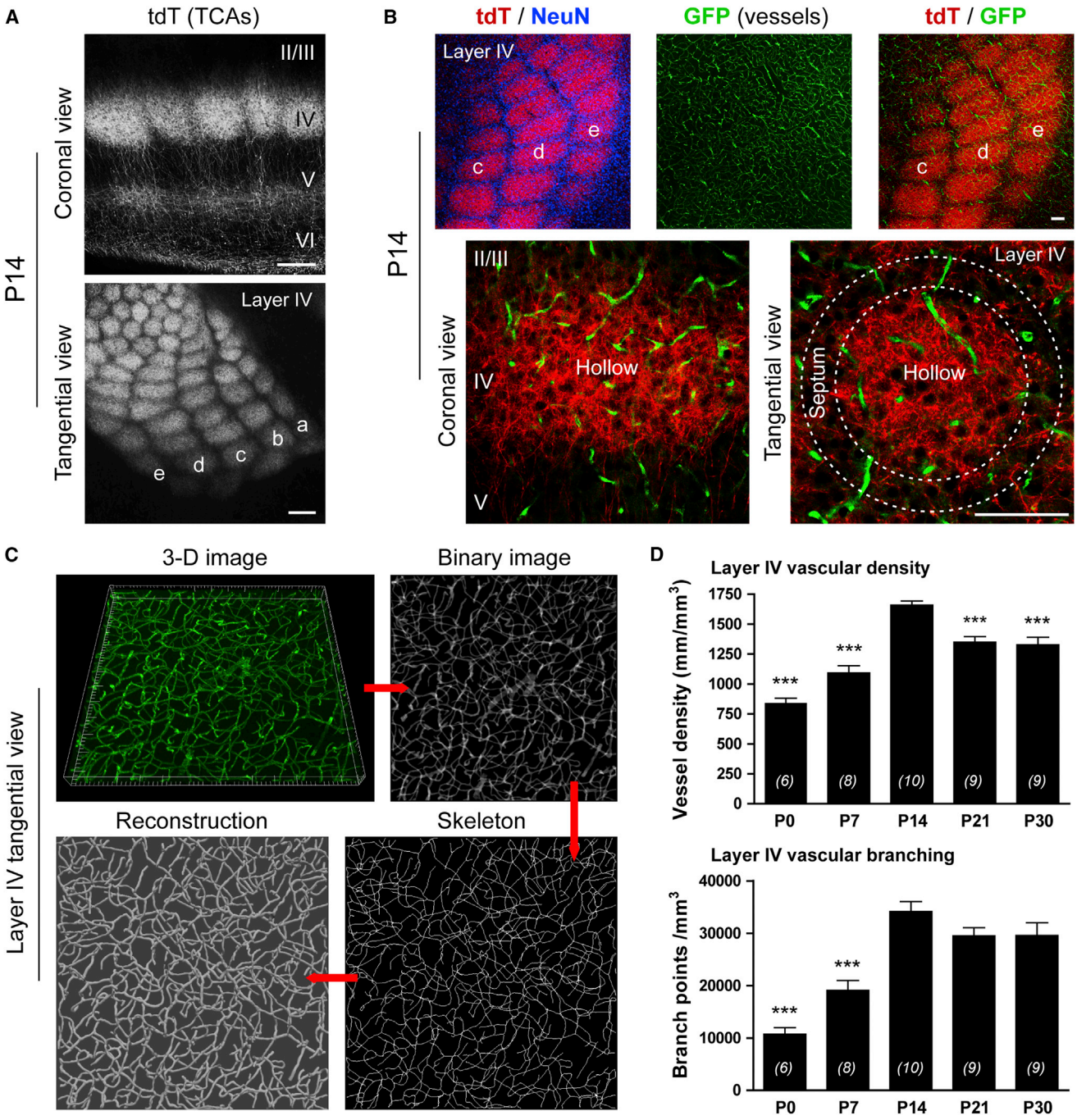

Figure 1. A Combination of Genetic, Imaging, and Computational Tools to Characterize Vascular Density and Branching in Layer IV of the Postnatal Mouse Barrel Cortex

(A) Thalamocortical axons (TCAs) in layer IV of the barrel cortex as labeled by tdTomato (tdT) expression driven by the serotonin transporter (Sert) promoter.

(B) A combination of three transgenic mouse lines (*Sert-Cre*, *tdT*$^{flox\text{-}stop\text{-}flox}$, and *Tie2-GFP*) allows for simultaneous visualization of TCAs (red) and brain vessels (green). Cortical neurons (neuronal nuclei NeuN immunostaining, blue in upper panel) are organized in barrel septa (outlined by dotted circles in lower panel).

(C) Overview of the image processing method used to analyze vascular structure (see Figure S3).

(D) Vascular density and branching in layer IV of the barrel cortex assayed between P0 and P30. Data are mean ± SEM. Numbers of animals are given in brackets. ***$p < 0.001$ (versus P14), one-way ANOVA, and Newman-Keuls post hoc test. Scale bars: 250 μm in (A) and 100 μm in (B).

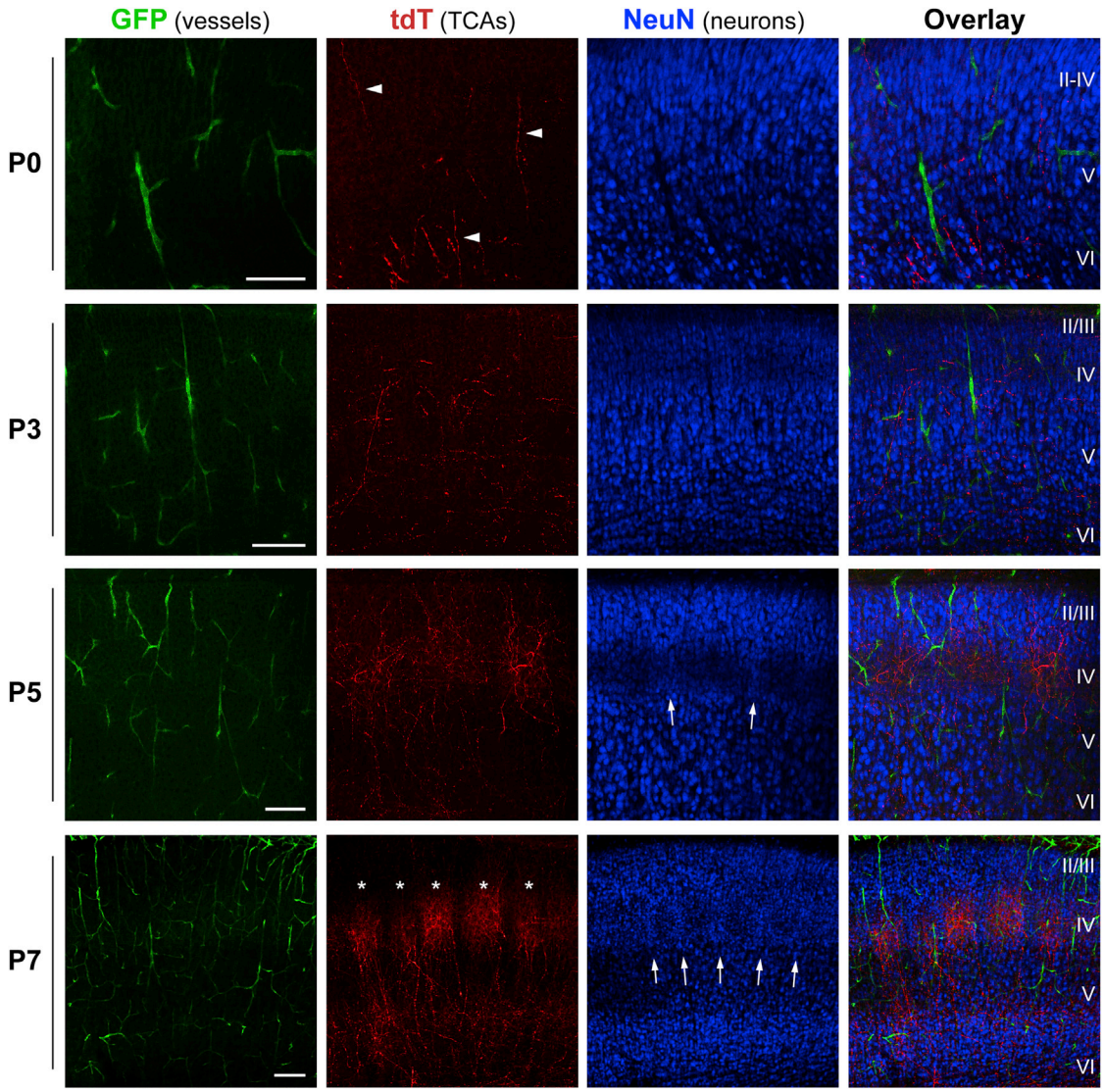

Figure 2. Early Postnatal Development (P0 to P7) of Neural and Vascular Modules in the Mouse Barrel Cortex

Coronal view of GFP-expressing vessels (green), tdT-expressing TCAs (red), and NeuN-immunostained cortical neurons (blue). TCAs (arrowheads) start to invade the cortex around birth, and clustering of TCAs and cortical neurons into barrel hollows (asterisks) and barrel septa (arrows), respectively, becomes clear at P7. To improve detection, sections were stained by anti-GFP and anti-tdT antibodies. Scale bars: 100 μm.

presynaptic ablation of both RIM1 and RIM2 in double knockout (RIM DKO^{Sert}) mice (Narboux-Nême et al., 2012), as confirmed here (Figures 4A, 4B, and S3A). At P14, a significant reduction of vascular density and branching was observed in barrel cortex layer IV of RIM DKO^{Sert} mice compared to littermate controls (Figure 4C). This phenotype was not detected in mice lacking only one RIM isoform in TCAs (RIM1 KO^{Sert} or RIM2 KO^{Sert}) in which layer IV barrel septa are formed correctly (Figures S3B and S3C). Moreover, there was no difference between RIM DKO^{Sert} and wild-type (WT) mice in the distribution of three major capillary categories based upon different diameters (Figure 4C), suggesting a uniform impairment of vascular growth in these mutants. Similar genetic experiments demonstrated previously that removal of RIMs in TCAs resulted in normal presynaptic ultrastructure, but neurotransmitter release was strongly impaired in layer IV where we examined the vasculature (Narboux-Nême et al., 2012). Therefore, these data demonstrate that reduction of neurotransmitter release at thalamocortical synapses results in both postsynaptic neuronal disorganization and decrease of vascular density and branching in layer IV of the cerebral cortex.

Reduction of Sensory-Related Neural Activity by Whisker Plucking Decreases Vascular Network Formation in Layer IV of the Barrel Cortex

We then aimed to further dissect the contribution of neural activity to vascular network formation. Whisker plucking is a convenient procedure to reduce sensory-related activity in layer

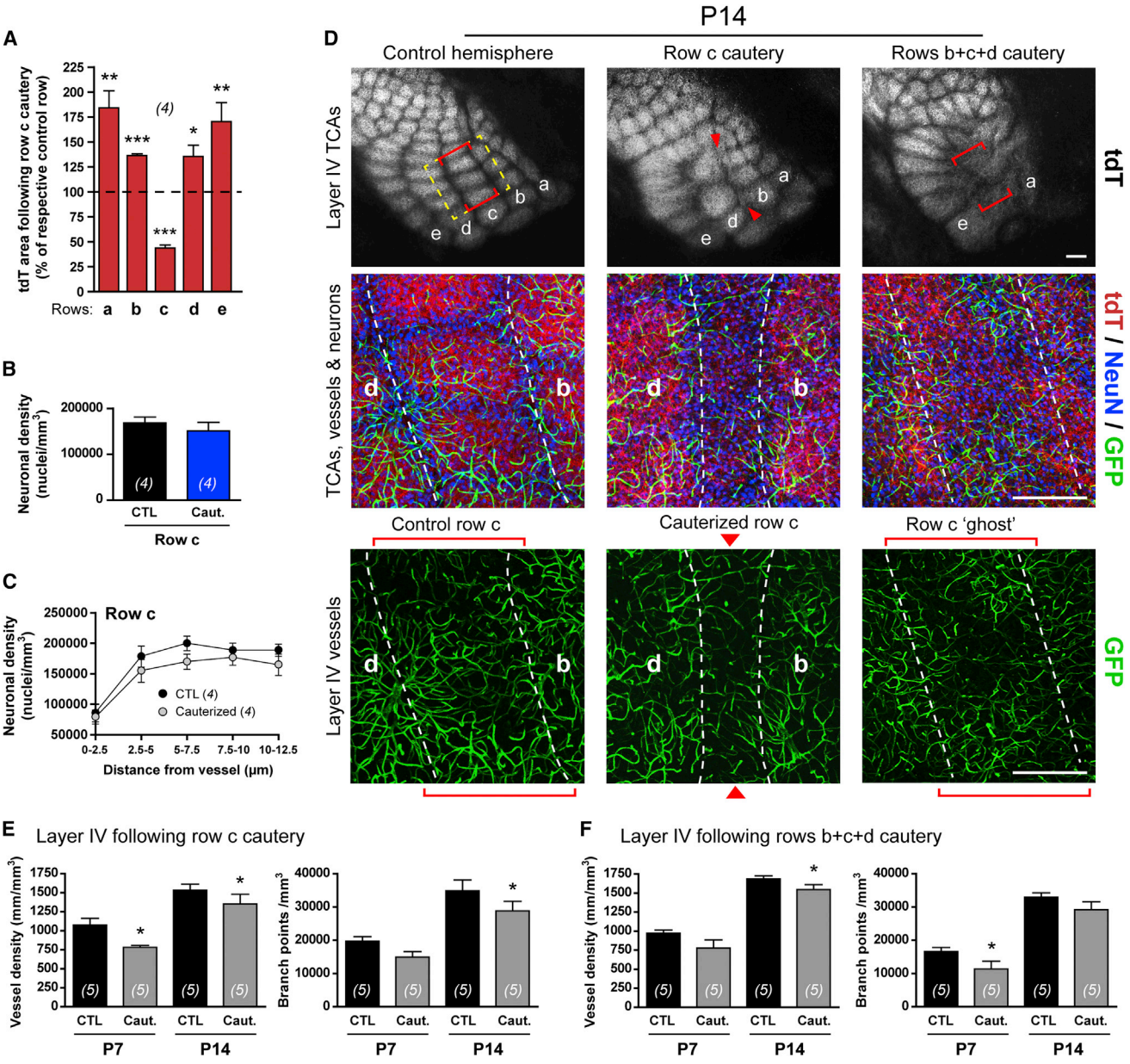

Figure 3. A Complete Deafferentation by Whisker Follicle Lesions Abolishes the Neuroarchitecture and Results in a Reduction of Vascular Density and Branching in Layer IV of the Barrel Cortex

(A–C) Analysis of neuronal parameters in barrel cortex layer IV following whisker row c lesion.

(A) Total area occupied by TCA clusters in each barrel row.

(B) Neuronal density within total row c volume.

(C) Relationship between neuronal density and distance from vessels in row c. No statistical difference was measured ($p > 0.05$, one-way ANOVA, and Newman-Keuls post hoc test).

(D) Effect of single (middle panels) or triple (right panels) whisker row lesion on neural and vascular structure in layer IV of the barrel cortex, in the ipsilateral (control) and contralateral (deprived) row c. In layer IV of the control (ipsilateral) hemisphere, TCAs and cortical neurons are organized into distinct rows. When whisker follicles are unilaterally cauterized (caut.) at birth, formation of their cortical representation is impaired (absence of axonal and neuronal patterning and expansion of surrounding rows). Field of view of vascular images in lower panels is outlined by a dotted square in upper left panel. Red brackets delimit the control row c. Red arrowheads point at the deafferented row c.

(E and F) Quantification of changes in layer IV vascular density and branching following single (E) and triple (F) whiskers row lesion compared to the control hemisphere. Data are mean ± SEM. Numbers of animals are given in brackets. *$p < 0.05$; **$p < 0.01$; ***$p < 0.001$, paired t test. Scale bars: 200 µm.

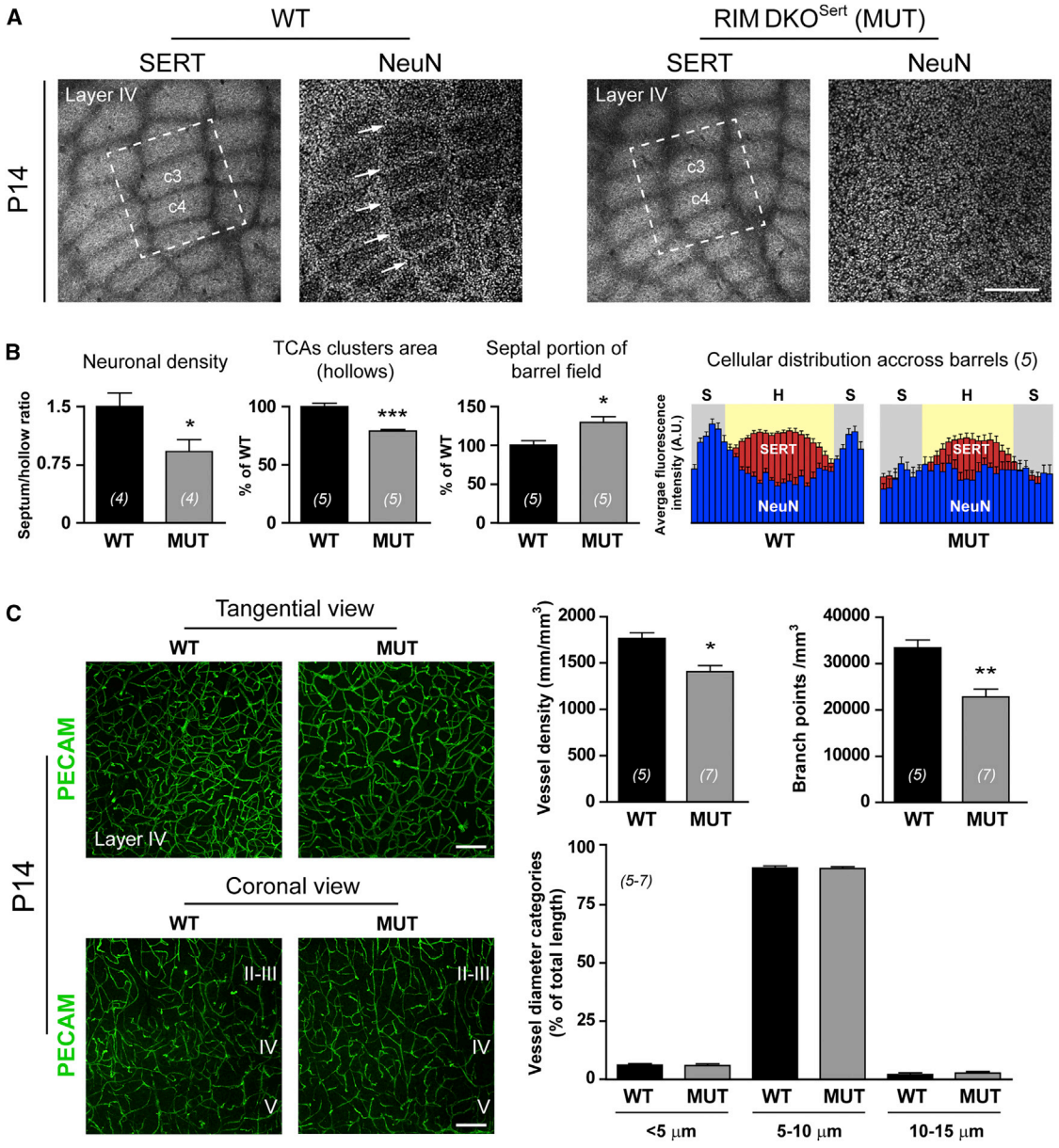

Figure 4. Reduction in Neurotransmitter Release by Genetic Ablation of RIMs at Thalamocortical Synapses Results in Postsynaptic Disorganization and Reduction of Vascular Network Formation in Layer IV of the Barrel Cortex

(A) Immunohistochemical stainings at P14 of TCAs with a serotonin transporter (SERT) antibody and of cortical neurons with a neuronal nuclei (NeuN) antibody (white arrows pointing at septa) from tangential sections in layer IV from RIM DKO^{Sert} (MUT) and WT mice. Dotted white squares indicate the field of view illustrated in (C) for vascular marker platelet endothelial cell adhesion molecule (PECAM) immunostaining.

(B) Quantification of the neuronal phenotype observed in RIM DKO^{Sert} compared to WT mice, including neuronal density, TCA clusters area, septal area, as well as distribution of NeuN-immunoreactive neurons (blue) and SERT-immunoreactive TCAs (red) across layer IV barrels c3 and c4 (average fluorescence intensity plots; bin size = 10 µm).

(C) Left: sample images (z projections) of PECAM-immunostained sections from tangential (upper panels) and coronal (lower panels) points of views. Right: 3D analysis of vessel density, branching, and diameter in layer IV vasculature from WT and RIM DKO^{Sert} mice. Data are mean ± SEM. Numbers of animals are given in brackets. *$p < 0.05$; **$p < 0.01$, one-way ANOVA (including other genotypes shown in Figure S3C) and Newman-Keuls post hoc test. Scale bars: 250 µm in (A) and 100 µm in (C).

IV without inflicting large-scale neuroarchitectural changes (Durham and Woolsey, 1978). Therefore, we performed early whisker plucking during the critical period for barrel cortex plasticity (P0 to P5) (Figures 5 and S2A). Vascular density and branching in the deprived hemisphere exhibited a significant reduction at P14 compared to the ipsilateral hemisphere, while neuronal distribution and density in layer IV were maintained in the deprived hemisphere (Figures 5A–5C and S4A). We then

plucked the whiskers after the P0–P5 critical period, between P14 and P21, a period when vascular density and branching normally decrease in WT mice (Figures 5C and S2A). This late plucking procedure led to a further decrease in vascular density and branching in layer IV of the contralateral hemisphere at P21 and P30 compared to the ipsilateral hemisphere (Figure 5C), whereas layer IV cytoarchitecture was preserved in the deprived hemisphere (Figure S4C). The reduction in vascular density and branching was specific to layer IV, as it was not evidenced in layer V (Figure S4D). Moreover, in both early and late whisker plucking, no change was detected in the distribution of the three main categories of capillaries with different diameters, suggesting a uniform impairment of vascular networks during sensory deprivation (Figure 5C). Since large-scale organization of neuronal cytoarchitecture was unchanged following whisker plucking, these data together demonstrate that reduction of sensory-related neural activity is sufficient to reduce vascular density and branching in the barrel cortex.

These results contrast with a recent study that found no reduction in vascular density in the early postnatal murine barrel cortex following whisker plucking (Whiteus et al., 2014). However, we noticed a major methodological difference in the image analysis between this study and ours. All our analyses have been done in 3D, whereas Whiteus et al. (2014) performed their analyses in 2D. To examine whether this methodological difference contributes to the divergent conclusions, we reanalyzed part of our early plucking data set using 2D methods. Vessel density and branching were quantified on maximal intensity z projections either from the whole z stack volume (Figure S4B, middle graphs) or from a fixed number of optical sections (Figure S4B, bottom graphs). Data from this analysis are expressed as vessel length and branch points per mm^2. In contrast to the 3D analysis, both 2D analyses failed to reveal any significant difference in vascular density and branching. The lower sensitivity of 2D analyses may be explained by a loss of information regarding vessel length in the third z dimension, as well as by the difficulty to count branch points and attribute them to a specific vessel in z projections.

Finally, to test whether the sensory-deprivation-induced reduction of vascular density and branching results from decreased angiogenesis, we assessed endothelial cell (EC) proliferation in vivo using 5-ethynyl-2′-deoxyuridine (EdU) incorporation. Following late whisker plucking, the number of proliferating ECs in the deprived hemisphere was significantly reduced compared to the ipsilateral hemisphere, while the number of proliferating non-ECs was unchanged (Figures 5D and S4E). Since angiogenesis is reduced following whisker plucking, these data demonstrate that sensory-related neural activity controls local vascular network formation in the early postnatal cerebral cortex.

Enhancement of Sensory Inputs by Whisker Stimulation Leads to an Increase in Vascular Density and Branching in Layer IV of the Barrel Cortex

To complement our sensory deprivation experiments, we performed a sensory enhancement paradigm by whisker stimulation (Figures 6 and S5), a procedure widely used to increase neural activity in layer IV of the barrel cortex (Lecrux et al., 2011). Whisker stimulation for 1 week starting at P14 led to significant increase in vascular density and branching in the contralateral hemisphere compared to the ipsilateral hemisphere at P21 (Figure 6A). Increased neural activation was evidenced by the increased number of c-Fos-positive nuclei in the stimulated barrel cortex (Figures 6B and S5B), while large-scale neuronal cytoarchitecture was maintained (Figure S5C). These results demonstrate that enhancement of sensory inputs to the barrel cortex increases vascular density and branching.

Reduction of Sensory-Related Neural Activity by Whisker Plucking Has No Impact on Astrocyte Distribution and Density in Layer IV of the Barrel Cortex

Since astrocytes have been shown to stimulate angiogenesis in vitro by releasing proangiogenic molecules in response to glutamate (Munzenmaier and Harder, 2000; Pozzi et al., 2005; Zhang and Harder, 2002), any impairment in the astroglial population might affect its ability to promote angiogenesis. Therefore, we examined the distribution and density of cortical astrocytes in two sensory deprivation paradigms (triple whisker row lesion and whisker plucking). Cerebral cortex astrocytes were labeled for aldehyde dehydrogenase 1 family member L1 (ALDH1L1), an astrocyte-specific marker with pan-astrocyte expression patterns (Cahoy et al., 2008; Molofsky et al., 2012). ALDH1L1-positive protoplasmic astrocytes were found throughout the brain parenchyma and enriched in layers II-III and IV of the cortex, with typical tubular arrangements corresponding to the lining of blood vessels by their fine processes or ''endfeet'' (Figures 7A, 7B, and S6). Astrocytes appeared accumulated within barrel hollows (Figures 7C and 7D) and in close contact with both TCAs and microvessels (Figure 7B). GFAP-positive fibrous astrocytes were found almost exclusively in the white matter, as previously described (Cahoy et al., 2008) (Figure S6). Following triple row lesion, both the distribution and cell density of astrocytes in the deprived hemisphere appeared significantly impaired compared to the ipsilateral hemisphere (Figure 7C). In contrast, no detectable differences in astrocyte distribution and cell density were found following whisker plucking (Figure 7D), a paradigm which also left the neuronal cytoarchitecture intact. These data demonstrate that large-scale organization of the astroglial population was unchanged following whisker plucking. However, it is still possible that astrocytes function to mediate the effects of neural activity on vascular network formation.

DISCUSSION

Our ability to manipulate sensory-related neural activity and to simultaneously examine both neuronal and vascular modules at the same location in barrel cortex layer IV enabled us to demonstrate that ''natural'' neural activity is necessary for vascular patterning and that changes in neural activity are sufficient to trigger alterations in vascular networks. The opposing impact of sensory deprivation and stimulation on vascular structure specifically in barrel cortex layer IV further demonstrates that neural activity normally promotes vascular network formation in this somatosensory pathway.

We demonstrate that changes in sensory-related neural activity are sufficient to control vascular plasticity, since vascular

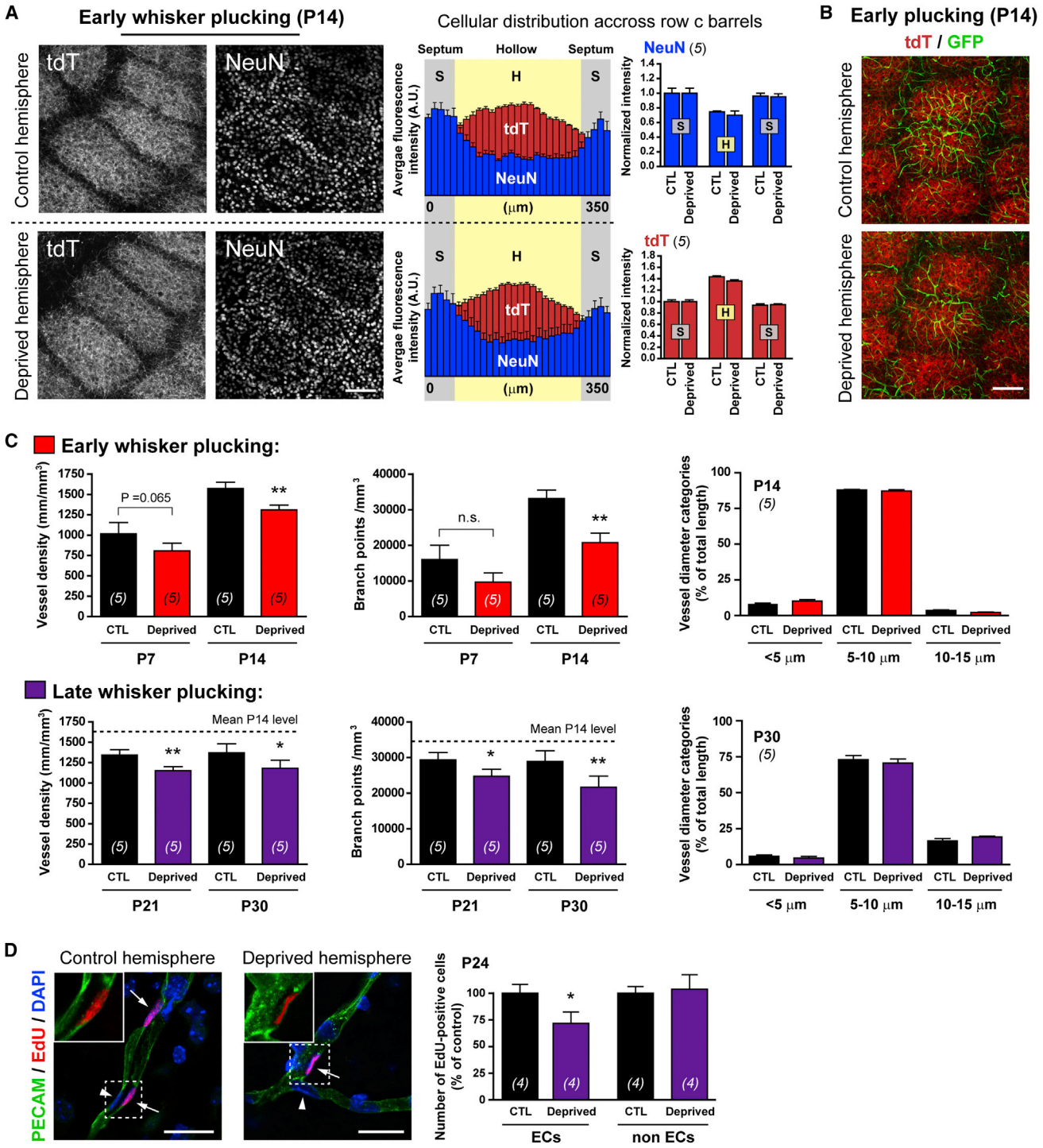

Figure 5. Reduction of Sensory-Related Neural Activity by Whisker Plucking Leads to a Reduction of Vascular Network Formation in Layer IV of the Barrel Cortex

(A) Illustrations (left) and quantifications (right) of neuron (NeuN, blue) and TCA (tdT, red) distribution across layer IV c3 and c4 barrels (average fluorescence intensity plots; bin size = 10 μm) (see Figure S4A). Data were also pooled for septa (S) and hollows (H).

(B) Organization of TCAs (tdT, red fluoresence) and cortical vessels (GFP, green fluorescence) following early whisker plucking.

(C) Early whisker plucking: Whiskers are plucked from P0 to P5, followed by analysis of vascular structure at P7 and P14. Late whisker plucking: Whiskers are plucked from P14 to P21, followed by analysis of vascular structure at P21 and P30 (see Figure S2A). Histograms are quantifications of changes in vessel density, branching, and diameter within barrel cortex layer IV.

(legend continued on next page)

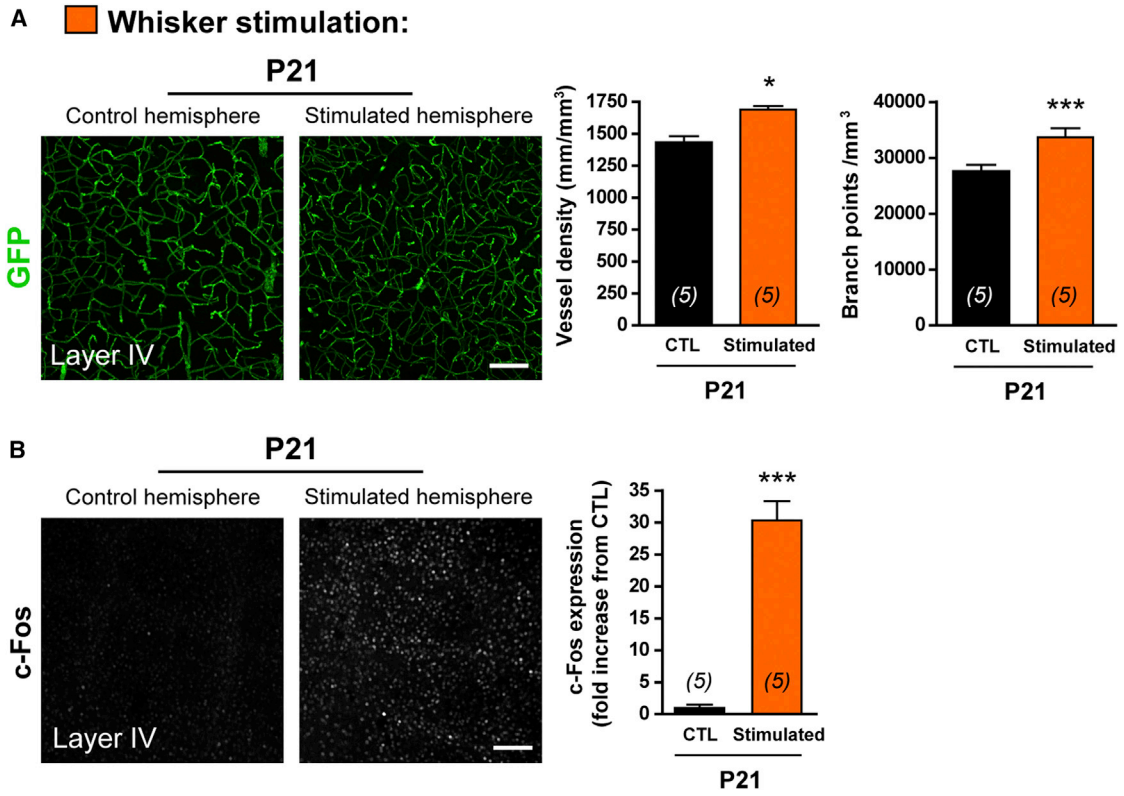

Figure 6. Enhancement of Sensory-Related Neural Activity by Whisker Stimulation Leads to an Increase in Vascular Density and Branching in Layer IV of the Barrel Cortex

(A) Effect of unilateral whisker stimulation for 1 week (see also Figure S2A) on vessel density and branching in layer IV in the ipsilateral (control) and contralateral (stimulated) hemispheres from the same animal.

(B) Effect of unilateral whisker stimulation on neuronal activation in layer IV, as assessed by c-Fos expression. Data are mean ± SEM. Numbers of animals are given in brackets. *$p < 0.05$; ***$p < 0.001$, paired t test. Scale bars: 100 μm.

patterning was affected in absence of large-scale neuronal and astroglial cytoarchitectural changes. Indeed, the reduction in sensory-driven inputs following both whisker lesion and whisker plucking led to a decrease in vascular network formation. In addition, the reduction in vascular density and branching is significantly higher following whisker plucking than following a wide whisker lesion ($p < 0.05$, unpaired t test), suggesting that large-scale neuronal cytoarchitectural changes did not produce additional vascular changes.

How does neural activity change the vascular structure? It is possible that sensory-related neural activity directly affects vascular patterning via the release of glutamate by TCAs or indirectly through pathways that are activated by synaptic transmission involving cortical interneurons and glial cells. It is well known that pyramidal excitatory neurons, inhibitory interneurons, and astrocytes are recruited by the whisker-to-barrel pathway (Lecrux et al., 2011) and that in turn they release vasoactive substances that control vascular tone and cerebral blood flow (Cauli and Hamel, 2010; Drake and Iadecola, 2007). Whether angiogenesis regulators are also released by these neuronal modules upon neural activity changes is yet to be examined. Astrocytes, being in close contact with both neuronal synapses and cerebral microvessels, are well positioned to mediate the effects of neural activity on vascular patterning. Indeed, in addition to their role in the control of blood flow (Attwell et al., 2010; Iadecola and Nedergaard, 2007; Lind et al., 2013) and in the maturation and function of neuronal circuits (Chung et al., 2013; Clarke and Barres, 2013; Eroglu et al., 2009), astrocytes are accurate sensors of neural activity and respond to glutamate by releasing proangiogenic lipids (epoxy-eicosa-trienoic acids, or EETs) at least as potent as VEGF (Munzenmaier and Harder, 2000; Potente et al., 2003; Pozzi et al., 2005; Zhang and Harder, 2002). Future studies could investigate the precise mechanisms through which neural activity controls the release of EETs in vivo and their effects on vascular patterning in the brain. Such proangiogenic mechanisms would likely play a role in improving the

(D) Assessment of proliferation of endothelial cells (ECs) and non-endothelial cells (non-ECs) by EdU incorporation following late whisker plucking over 10 days (see Figure S4E). Proliferating endothelial nuclei, that are positive for EdU (red), are indicated by arrows; nonproliferating endothelial nuclei are indicated by arrowheads. Top-left insets are a magnification of the area delimited by dotted squares. Data are mean ± SEM. Numbers of animals are given in brackets. *$p < 0.05$; **$p < 0.01$, paired t test (n.s., not significant). Scale bars: 100 μm in (A) and (B) and 20 μm in (D).

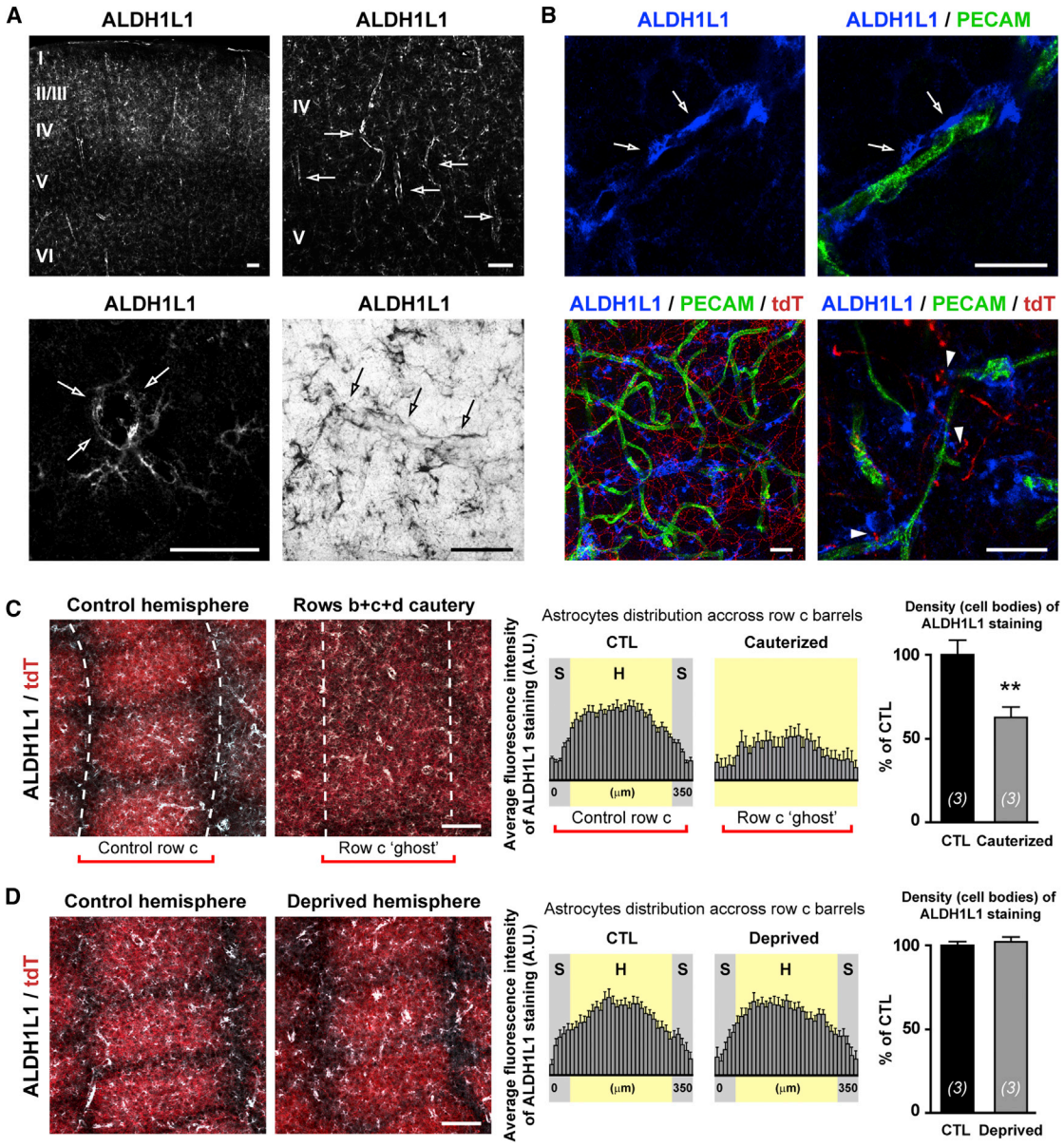

Figure 7. The Distribution and Cell Density of Barrel Cortex Astrocytes Are Affected by Whisker Lesion, but Not by Whisker Plucking

(A) Distribution of protoplasmic astrocytes as revealed by ALDH1L1 immunostaining. Low and high magnifications are provided in upper and lower panels, respectively. Arrows designate tubular arrangements of astrocytic processes (endfeets).

(B) Double (upper panels) and triple (lower panels) immunostainings showing ALDH1L1-positive astrocytes (blue) in close contact with vessels (green) and TCAs (red). Arrows designate astrocytic endfeet lining blood vessels. Examples of close encounter between astrocytes, vessels, and nerves are indicated by arrowheads in lower right panel.

(C and D) Effect of triple whisker row lesion (C) and late whisker plucking (D) on the cellular distribution (average fluorescence intensity plots, bin size of 10 μm, middle panels) and density (right histograms) of barrel cortex astrocytes in layer IV. Data are mean ± SEM. Numbers of animals are given in brackets. **$p < 0.01$, paired t test. Scale bars: 50 μm in (A), 25 μm in (B), and 100 μm in (C) and (D).

balance between metabolic demand and energy supply (Blinder et al., 2013; Riddle et al., 1993).

We demonstrate by a combination of three paradigms of sensory deprivation together with neural activity enhancement that, under physiological conditions, neural activity normally promotes vascular network formation. In contrast, Whiteus et al. (2014) found a severe reduction of angiogenesis in the motor cortex after treadmill exercise (45 min, three times daily for 5 days) and in the auditory cortex following persistent and repetitive auditory stimulation (over 10 hr daily, from P15 to P25). These hyperactivation paradigms result in widespread inhibition or stimulation in a variety of brain areas. Thus, it is

hard to establish a direct physiological link between local neural activity and changes in vascular patterning using these paradigms.

The finding that local neural activity promotes the formation of vascular networks in the cerebral cortex expands our understanding of neurovascular interactions and is relevant in the context of blood-oxygen-level-dependent (BOLD) functional imaging. In light of the reduced vascular bed following sensory deprivation, additional vascular parameters should be taken into consideration to improve accuracy of BOLD functional imaging studies in sensory-deprived brain regions (e.g., in blindness or deafness). Indeed, it has recently been demonstrated that blood flow, the basis of BOLD imaging, is not only not solely controlled by arteriole smooth muscle but also at the capillary level by pericytes (Hall et al., 2014; Hamilton et al., 2010).

Our results obtained in the early postnatal brain also lead us to hypothesize that sensory stimulation may be beneficial to enhance angiogenesis, a paradigm that could potentially be used to prevent or treat early-life ischemic conditions. Indeed, the brain is vulnerable to ischemia, particularly during critical developmental periods when insults trigger irreversible deficits, leading to syndromes such as cerebral palsy (Reddihough and Collins, 2003). Mouse models of perinatal stroke (Tsuji et al., 2013; Vexler et al., 2006) could be used to test this possibility, and whisker stimulation has been shown to enhance endothelial cell proliferation in the ischemic adult barrel cortex (Li et al., 2011; Whitaker et al., 2007).

Finally, our data suggest that the postnatal maturation of brain vascular networks not only relies on genetic programs but is also controlled by environmental stimuli. It will be important to examine whether neural activity plays a role in the control of cerebrovascular patterning in the healthy brain during adulthood, when neuronal structural plasticity is present but limited.

EXPERIMENTAL PROCEDURES

Animals

Transgenic mouse lines crossed for simultaneous imaging of TCAs and brain vessels were as follows: *Sert-Cre* (MMRRC:017260-UCD; mixed FVB/B6/129 genetic background), *tdTomato*$^{flox\text{-}stop\text{-}flox}$ (Jackson laboratory, strain 007905; mixed B6/129 background), and *Tie2-GFP* (Jackson laboratory, strain 003658; FVB/N background). For thalamic ablation of RIM1 and RIM2 proteins, *Rim1*$^{flox/flox}$-*Rim2*$^{flox/flox}$ mice on a mixed B6/129 background (Kaeser et al., 2011; Kaeser et al., 2008) were crossed with the *Sert-Cre* line. *Sert-Cre*$^{+/-}$; *Rim1*$^{flox/+}$-*Rim2*$^{flox/+}$ mice were then bred with *Rim1*$^{flox/flox}$-*Rim2*$^{flox/flox}$ mice to obtain *Sert-Cre*$^{+/-}$;*Rim1*$^{flox/flox}$-*Rim2*$^{flox/flox}$ (RIM DKO^{Sert}), *Sert-Cre*$^{+/-}$; *Rim1*$^{flox/flox}$-*Rim2*$^{flox/+}$ (RIM1 KO^{Sert}), and *Sert-Cre*$^{+/-}$;*Rim1*$^{flox/+}$-*Rim2*$^{flox/flox}$ (RIM2 KO^{Sert}) mice. Mice were raised in standard cages. All animals were treated according to institutional and NIH guidelines approved by IACUC at Harvard Medical School.

Manipulations of Sensory Inputs

Whisker Lesions

Adapted from previous reports (Datwani et al., 2002; Woolsey and Wann, 1976), newborn mice (P0) were anesthetized by hypothermia and the central row (c) or the rows b, c, and d of large whiskers were cauterized under a surgical microscope using an electrosurgery unit (ART-E1, Bonart Co., Keelung City, Taiwan). Neonates were then slowly warmed up on a heating pad (33°C, 20 min), returned to their mothers, and euthanized at P7 or P14. The precision and extent of lesions could be verified in the cortex following immunostainings (see below), and mice with imperfect lesions were excluded from the study.

Early Whisker Plucking

Newborns were anesthetized as above, and all large whiskers were plucked from the right side of the snout by applying a gentle tension to the base of the vibrissae (Brown and Dyck, 2003; Fox, 1992; Kossut, 1985). Care was taken to prevent damage to the whisker follicle. Neonates were slowly warmed up, returned to their mothers, and euthanized at P7 or P14. In order to maintain sensory deprivation during the critical period for plasticity (P0–P5), vibrissae were checked for regrowth and replucked if necessary until P5.

Late Whisker Plucking

P14 animals were anesthetized using isoflurane (3% induction, 1.5%–2% maintenance, in 100% oxygen), and all large whiskers were plucked as above. Mice were returned to their mothers and euthanized at P21 or P30. For assessment of cell proliferation in vivo, all large whiskers were plucked from P14 to P24. Vibrissae were checked for regrowth every other day until sacrifice.

Whisker Stimulation

Adapted from previous studies (Filipkowski et al., 2000; Lecrux et al., 2011), pups where first habituated to the experimental conditions and were then subjected to daily whisker stimulation for 8 days (P14 to P21). Each day, pups where gently restrained on the top of a plastic cylinder, and their right whiskers were manually stimulated for 15 min (3 to 4 Hz) using a paint brush. In our case, since whisker plucking led to reduction of vascular network density and branching, the contralateral whiskers were left intact. Sham controls were manipulated but not stimulated. Mice were euthanized at P21, 1 hr after the last stimulation.

Immunohistochemistry

For all experiments except in vivo EdU incorporation (see below), mice were euthanized at experimental endpoints by cervical dislocation, and the brain was removed from the skull. For a coronal view of cerebral structures, the whole brain was fixed by immersion in 4% paraformaldehyde (PFA) overnight at 4°C. For a tangential view of cortical layers, the cortex was dissected in ice-cold PBS, flattened between two glass slides, and fixed by immersion in 4% PFA overnight at 4°C. Fixation by immersion allows all brains from each experimental group to be fixed exactly the same way and at the same time, reducing interanimal variability. Fixed brains and flatten cortices were then rinsed in PBS, embedded in 2% agarose in PBS, and cut coronally (whole brain) or tangentially (flatten cortex) into serial, thick sections (50 μm for 2D illustrations; 120 μm for 3D vascular reconstructions) using a vibratome (Leica VT1000S). Sections were blocked with 10% horse serum, permeabilized with 0.2% Triton X-100, and incubated overnight with one or a mixture of the following primary antibodies: rabbit α-GFP (1:1,000; A-11122, Life Technologies), α-DsRed (1:500; 632496, Clontech), α-c-Fos (1:250; sc-52, Santa Cruz Biotechnoloy, Inc), α-ALDH1L1 (1:500; ab87117, Abcam), guinea pig α-NeuN (1:1000; ABN90, EMD Millipore), rat α-PECAM-1 (1:200; 553370, BD PharMingen), and goat α-SERT (1:500; sc-1458, Santa Cruz Biotechnoloy, Inc), followed by species-specific 568/488 Alexa Fluor-conjugated (Invitrogen) or Cy™5-conjugated (Jackson ImmunoResesarch) secondary antibodies (1:300). Slides were mounted in Fluoromount G (EMS) and visualized by epifluorescence or confocal microscopy.

In Vivo Assessment of Cell Proliferation

Four mice were subjected to a slightly modified "late plucking" paradigm for a 10-day deprivation. All large whiskers were plucked from P14 to P24. To assess cell proliferation in vivo, we used the sensitive method of EdU incorporation. EdU detection only requires fast chemical staining compatible with high-resolution immunohistochemistry (Cappella et al., 2008; Salic and Mitchison, 2008). Adapted from previous reports (Salic and Mitchison, 2008; Zeng et al., 2010), mice received EdU injections (100 μg/day, in PBS, intraperitoneally) from P14 to P23 and were euthanized at P24 by transcardial perfusion with 4% PFA under deep anesthesia. Their brain was post-fixed in 4% PFA, cryoprotected in 30% sucrose, and embedded for cryostat sectioning. EdU was detected on 40-μm-thick sections using a Click-iT Alexa Fluor 594 EdU Imaging Kit (C10340, Life Technologies) following manufacturer's protocol. Briefly, slides were washed in 3% BSA in PBS, permeabilized with 0.5% Triton, washed again in 3% BSA-PBS, and then incubated with the Click-iT reaction cocktail. Slides were then washed in 3% BSA-PBS and processed for

immunohistochemistry to label vessels (PECAM-1) and nuclei (DAPI). The proportions of proliferating ECs and non-ECs were assessed by manually counting EdU-positive and EdU-negative nuclei in the ipsilateral versus contralateral hemispheres from confocal images (60× oil immersion objective, 1× zoom, 1 μm optical sections) using ImageJ Cell Counter (n = 4, three brain sections per animal, five images per hemisphere on each section).

Image Acquisition

Immunostained sections were examined under a laser scanning confocal microscope (Olympus FluoView™ FV1000). For single image illustrations, maximal intensity z projections were obtained from 5 to 10 μm z stacks acquired using either a 4×, 10×, 20×, or 60× objective (1 μm optical sections, 1× zoom). For 3D reconstruction of vascular networks in flattened cortex tangential sections, layer IV of the posteromedial barrel field was located using tdT fluorescence under a 10× objective, and then 50- to 70-μm-deep z stacks (1 μm optical sections, 1× zoom) were acquired for the vascular GFP signal in the core of layer IV using a 20× objective (Figure S1C).

For temporal characterization of layer IV vasculature (Figure 1D), adjacent z stacks covering the width of the barrel field were acquired in the right hemisphere. For whisker lesion experiments (Figure 3), one z stack centered over barrel row c was acquired in each brain side: in the control hemisphere (ipsilateral to the lesion) and in the lesioned (contralateral) hemisphere (Figure S2C). For conditional loss of RIM proteins (Figure 4), three adjacent z stacks covering the width of the barrel field were acquired in the right hemisphere from immunostained sections of mutant and littermates control mice. For whisker plucking and stimulation experiments (Figures 5 and 6), three adjacent z stacks covering the width of the barrel field were acquired in the control and manipulated hemispheres (Figure S2D).

Images and illustrations were processed using ImageJ (NIH), Adobe Photoshop CS6, and Adobe Illustrator CS6.

Computational Analysis of Cortical Vasculature

Data Collection

For whisker lesion experiments, the volume of the row c in the intact hemisphere, delimited by boundaries between neuronal septa (NeuN), was considered as the internal control (Figures 3D and S2C). In the contralateral hemisphere following single row lesion, layer IV vessels were analyzed within the "lesioned volume" (Figure S2C), whose borders are defined by neuronal septa (NeuN) from rows b and d. Following triple row lesion, layer IV vessels were analyzed within the row c "ghost" volume (Figure S2C), which corresponds to a projection of the control row c volume over the mispatterned field in the deprived hemisphere. Dotted lines in Figures 3D and S2C represents either the anatomical borders of controls and lesioned row c or the borders of the projected row c "ghost" volume.

All vascular measurements from raw z stack files were analyzed by a person blind to experimental conditions.

Computational Morphometric Analysis of 3D Vascular Images

The algorithms used to process the stacks were implemented in Python 2.7 using the following python modules: Numpy, Scipy, Matplotlib, Opencv2, Igraph, and Scikit-Image.

Step 1: Each image was smoothed in order to reduce noise by using the Gradient Anisotropic Diffusion filter from SimpleITK software (http://www.simpleitk.org/). An adaptive thresholding algorithm (Gonzalez and Woods, 2007) with a window size of 100 μm was applied to each image in the z stack. If the intensity of a pixel was greater than the mean intensity of pixels inside the window centered on the concerned pixel, this pixel was classified as belonging to a vessel. The resulting binary image may contain pixels incorrectly classified as vessel pixels. This was corrected by deleting image components smaller than 500 μm^3 (Shapiro and Stockman, 2001). Background pixels may remain inside vessels (i.e., holes). In order to fill such holes, background components smaller than 100 μm^3 were removed. The final binary image was obtained by doing a closing operation (Dougherty and Lotufo, 2003) with a 6-pixel-wide disk.

Step 2: Skeletonization has been used previously for geometric characterization of biological shapes (Cesar and Costa, 1999; Meng et al., 2008; Rafelski et al., 2012; Viana et al., 2009). In the current work, the skeleton of the blood vessels was obtained by a thinning algorithm (Palàgyi and Kuba, 1998) and was then represented as a network. Each pixel having three or more neighbors was classified as a branching point, and pixels having only one neighbor were identified as terminal points. The positions of branching and termination points, as well as all points of the segments, were stored for analysis.

Step 3: Noise and irregularities in vascular structure may generate some spurious short segments. An iterative algorithm was applied to sequentially remove them. Segments smaller than 10 μm were recurrently erased, starting from the endpoints of the skeletons. The length of each segment was then estimated by using a differential estimate of the arc length (Costa and Cesar, 2009). We also measured the number of branching points in each z stack. Finally, in order to validate the analysis, we created 3D images containing both the original image and the final skeletons and verified that the obtained skeletons were accurately representing the original blood vessel structure.

Step 4: For vessel radius estimation, each skeleton segment was linearly interpolated and smoothed. Each point of the transformed segment was associated to a plane that is perpendicular to the segment, passing through the point. This plane was used to find the cross-section of the binary vessel image at the point. The area A of the cross-section defines the equivalent radius of the blood vessel at the point trough the formula $r = \sqrt{A/\pi}$, which is the radius of a disk of area A. We eliminate points that are closer than 3 μm to a termination or branching of the segment. Finally, the median of the radius calculated on the remaining points was associated to the whole segment.

Computational Morphometric Analysis of 2D Vascular Images

Two analyses were done in the early plucking data set (three randomly chosen animals) to quantify vessel density and branching in 2D. These two analyses differ one another on the number of z stack planes used to create the 2D image. In the first one, we used the whole z stack volume for the 2D z projection. In the second, we first extracted a region of interest (ROI) from the z stacks. This region was centered in the middle of the z stack and was 15 μm deep. For both analyses, the respective 2D image was obtained by doing a maximum intensity z projection of the extracted region. The algorithm to characterize the 2D images was similar to that used for 3D images, with the only difference being the binarization procedure, which is described in step 1 of the previous section. For the 2D analysis, we used a window size of 220 μm for the adaptive thresholding, and components smaller than 100 μm^3 were removed.

Estimation of Neuronal Density and Its Relationship to Vessels in 3D

The 3D NeuN-positive neuronal nuclei images were first smoothed using a Gaussian filter. Then, an adaptive threshold with a window size of 100 μm was applied to each plane of the z stack. Components smaller than 150 μm^3 were removed. Nuclei that were merged into a single component were separated by detecting their respective centers, which was done by using the distance transform (Costa and Cesar, 2009). The result of this procedure is a new image containing the centroid of each neuronal nucleus.

The neuronal density was estimated using the binary blood vessel image and the centroids found in the previous step. The binary image was used as a reference to define shells around the blood vessels, each shell containing all image points with distance larger than x and smaller than x + Δx from the border of the binary blood vessel structure. The neuronal density for the shell was then calculated as the number of neuron centroids inside the shell divided by the shell volume. The width of the shell was set as Δx = 2.5 μm (Travençolo et al., 2007).

Cell Counting and Average Intensity Plots

Quantifications were adapted from previous reports (Mangin et al., 2012; Narboux-Nême et al., 2012).

Confocal images (20× objective, 1 μm optical sections, 1× zoom) and maximal intensity z projections (five optical sections) were used for quantification. Using the Cell Counter plugin of ImageJ (NIH), we obtained the number of neurons by counting NeuN-positive nuclei and the number of astrocytes by counting the number of ALDH1L1-positive soma colocalizing with DAPI nuclear staining in the ROI (e.g., barrel row, barrel hollow, or barrel septa). All quantifications were done on a ROI that includes both row c barrels c3 and c4 that display similar size. The interbarrel "septal" area was defined using tdT-positive TCAs as the total area of ROI minus the sum of tdT-positive clusters. Densities were obtained by dividing the number of cells by the area of the ROI (mean of c3 and c4 barrels for neurons, whole-row c and row c ghost for astrocytes).

Average intensity plots were done using the Plot Profile function in ImageJ (NIH). We either show average image profile plots in which intensity value of several adjacent pixels are averaged (10 μm per bin) or average profile plots profiles where values from septa and hollows are pooled.

Statistical Methods

Vascular morphological features obtained blindly from the computational analysis were regrouped and averaged for each animal to obtain an individual value (score). Scores obtained for each parameter for each animal were then averaged within experimental groups. Statistical analyses were performed using Prism4 (GraphPad Software). Multiple group comparisons were analyzed using a one-way ANOVA followed by a Newman-Keuls post hoc test. Two group comparisons were analyzed using paired or unpaired Student's t test. Data reported are mean ± SEM. $p < 0.05$ was considered statistically significant.

SUPPLEMENTAL INFORMATION

Supplemental Information includes six figures and can be found with this article online at http://dx.doi.org/10.1016/j.neuron.2014.07.034.

ACKNOWLEDGMENTS

We thank Drs. Christopher Harvey and Jonathan Cohen, and members of the Gu laboratory, for constructive comments on the manuscript; Dr. Susan Dymecki for providing the Slc6a4-Cre mouse; Drs. Lisa Goodrich and Bernardo Sabatini for sharing their lab equipment; the Neurobiology Imaging Facility in the department of Neurobiology at Harvard Medical School (facility supported in part by the Neural Imaging Center as part of an NINDS P30 Core Center grant #NS072030) and the Enhanced Neuroimaging Core at Harvard NeuroDiscovery Center for helping with confocal imaging; and Lydia Bickford for technical assistance. This work was supported by the Mahoney postdoctoral fellowship (B.L.), the Goldenson and Lefler postdoctoral fellowships (A.B.Z), by FAPESP grant 2011/22639-8 (C.H.C.), FAPESP grant 11/50761-2, CNPQ grant 304351/2009-1 (L.d.F.C.), grant K01DA029044 from NIH/NIDA (P.S.K.), and by the following grants to C.G.: Harvard/MIT Joint Research Grants Program in Basic Neuroscience, Sloan research fellowship, the Genise Goldenson fund, the Freudenberger award, and NIH grant R01NS064583.

Accepted: July 18, 2014
Published: August 21, 2014

REFERENCES

Attwell, D., Buchan, A.M., Charpak, S., Lauritzen, M., Macvicar, B.A., and Newman, E.A. (2010). Glial and neuronal control of brain blood flow. Nature *468*, 232–243.

Ben-Zvi, A., Lacoste, B., Kur, E., Andreone, B.J., Mayshar, Y., Yan, H., and Gu, C. (2014). Mfsd2a is critical for the formation and function of the blood-brain barrier. Nature *509*, 507–511.

Black, J.E., Sirevaag, A.M., and Greenough, W.T. (1987). Complex experience promotes capillary formation in young rat visual cortex. Neurosci. Lett. *83*, 351–355.

Black, J.E., Isaacs, K.R., Anderson, B.J., Alcantara, A.A., and Greenough, W.T. (1990). Learning causes synaptogenesis, whereas motor activity causes angiogenesis, in cerebellar cortex of adult rats. Proc. Natl. Acad. Sci. USA *87*, 5568–5572.

Blinder, P., Tsai, P.S., Kaufhold, J.P., Knutsen, P.M., Suhl, H., and Kleinfeld, D. (2013). The cortical angiome: an interconnected vascular network with noncolumnar patterns of blood flow. Nat. Neurosci. *16*, 889–897.

Brown, C.E., and Dyck, R.H. (2003). Experience-dependent regulation of synaptic zinc is impaired in the cortex of aged mice. Neuroscience *119*, 795–801.

Cahoy, J.D., Emery, B., Kaushal, A., Foo, L.C., Zamanian, J.L., Christopherson, K.S., Xing, Y., Lubischer, J.L., Krieg, P.A., Krupenko, S.A., et al. (2008). A transcriptome database for astrocytes, neurons, and oligodendrocytes: a new resource for understanding brain development and function. J. Neurosci. *28*, 264–278.

Cappella, P., Gasparri, F., Pulici, M., and Moll, J. (2008). A novel method based on click chemistry, which overcomes limitations of cell cycle analysis by classical determination of BrdU incorporation, allowing multiplex antibody staining. Cytometr. A *73*, 626–636.

Carmeliet, P., and Tessier-Lavigne, M. (2005). Common mechanisms of nerve and blood vessel wiring. Nature *436*, 193–200.

Cauli, B., and Hamel, E. (2010). Revisiting the role of neurons in neurovascular coupling. Front. Neuroenergetics *2*, 9.

Cesar, R.M., Jr., and Costa, L.D. (1999). Computer-vision-based extraction of neural dendrograms. J. Neurosci. Methods *93*, 121–131.

Chung, W.S., Clarke, L.E., Wang, G.X., Stafford, B.K., Sher, A., Chakraborty, C., Joung, J., Foo, L.C., Thompson, A., Chen, C., et al. (2013). Astrocytes mediate synapse elimination through MEGF10 and MERTK pathways. Nature *504*, 394–400.

Clarke, L.E., and Barres, B.A. (2013). Emerging roles of astrocytes in neural circuit development. Nat. Rev. Neurosci. *14*, 311–321.

Costa, L.F., and Cesar, R.M., Jr. (2009). Shape classification and analysis: theory and practice, Second Edition. (Boca Raton: CRC Press).

Datwani, A., Iwasato, T., Itohara, S., and Erzurumlu, R.S. (2002). Lesion-induced thalamocortical axonal plasticity in the S1 cortex is independent of NMDA receptor function in excitatory cortical neurons. J. Neurosci. *22*, 9171–9175.

Dougherty, E.R., and Lotufo, R.A. (2003). Hands-on Morphological Image Processing, First Edition. (Bellingham: SPIE Publications).

Drake, C.T., and Iadecola, C. (2007). The role of neuronal signaling in controlling cerebral blood flow. Brain Lang. *102*, 141–152.

Durham, D., and Woolsey, T.A. (1978). Acute whisker removal reduces neuronal activity in barrels of mouse SmL cortex. J. Comp. Neurol. *178*, 629–644.

Eroglu, C., Allen, N.J., Susman, M.W., O'Rourke, N.A., Park, C.Y., Ozkan, E., Chakraborty, C., Mulinyawe, S.B., Annis, D.S., Huberman, A.D., et al. (2009). Gabapentin receptor alpha2delta-1 is a neuronal thrombospondin receptor responsible for excitatory CNS synaptogenesis. Cell *139*, 380–392.

Erzurumlu, R.S., and Gaspar, P. (2012). Development and critical period plasticity of the barrel cortex. Eur. J. Neurosci. *35*, 1540–1553.

Filipkowski, R.K., Rydz, M., Berdel, B., Morys, J., and Kaczmarek, L. (2000). Tactile experience induces c-fos expression in rat barrel cortex. Learn. Mem. *7*, 116–122.

Fox, K. (1992). A critical period for experience-dependent synaptic plasticity in rat barrel cortex. J. Neurosci. *12*, 1826–1838.

Fu, M., and Zuo, Y. (2011). Experience-dependent structural plasticity in the cortex. Trends Neurosci. *34*, 177–187.

Gelfand, M.V., Hong, S., and Gu, C. (2009). Guidance from above: common cues direct distinct signaling outcomes in vascular and neural patterning. Trends Cell Biol. *19*, 99–110.

Gonzalez, R.C., and Woods, R.E. (2007). Digital Image Processing, Third Edition. (New Jersey: Prentice Hall).

Hall, C.N., Reynell, C., Gesslein, B., Hamilton, N.B., Mishra, A., Sutherland, B.A., O'Farrell, F.M., Buchan, A.M., Lauritzen, M., and Attwell, D. (2014). Capillary pericytes regulate cerebral blood flow in health and disease. Nature *508*, 55–60.

Hamel, E. (2006). Perivascular nerves and the regulation of cerebrovascular tone. J. Appl. Physiol. (1985) *100*, 1059–1064.

Hamilton, N.B., Attwell, D., and Hall, C.N. (2010). Pericyte-mediated regulation of capillary diameter: a component of neurovascular coupling in health and disease. Front. Neuroenergetics *21*, http://dx.doi.org/10.3389/fnene.2010.00005.

Harb, R., Whiteus, C., Freitas, C., and Grutzendler, J. (2013). In vivo imaging of cerebral microvascular plasticity from birth to death. J. Cereb. Blood Flow Metab. *33*, 146–156.

Harris, R.M., and Woolsey, T.A. (1981). Dendritic plasticity in mouse barrel cortex following postnatal vibrissa follicle damage. J. Comp. Neurol. *196*, 357–376.

Iadecola, C., and Nedergaard, M. (2007). Glial regulation of the cerebral microvasculature. Nat. Neurosci. *10*, 1369–1376.

Kaeser, P.S., Kwon, H.B., Chiu, C.Q., Deng, L., Castillo, P.E., and Südhof, T.C. (2008). RIM1alpha and RIM1beta are synthesized from distinct promoters of the RIM1 gene to mediate differential but overlapping synaptic functions. J. Neurosci. *28*, 13435–13447.

Kaeser, P.S., Deng, L., Wang, Y., Dulubova, I., Liu, X., Rizo, J., and Südhof, T.C. (2011). RIM proteins tether Ca2+ channels to presynaptic active zones via a direct PDZ-domain interaction. Cell *144*, 282–295.

Katz, L.C., and Shatz, C.J. (1996). Synaptic activity and the construction of cortical circuits. Science *274*, 1133–1138.

Kleinfeld, D., and Deschênes, M. (2011). Neuronal basis for object location in the vibrissa scanning sensorimotor system. Neuron *72*, 455–468.

Kossut, M. (1985). Effects of sensory denervation and deprivation on a single cortical vibrissal column studied with 2-deoxyglucose. Physiol. Bohemoslov. *34* (*Suppl*), 79–83.

Lecrux, C., and Hamel, E. (2011). The neurovascular unit in brain function and disease. Acta Physiol. (Oxf.) *203*, 47–59.

Lecrux, C., Toussay, X., Kocharyan, A., Fernandes, P., Neupane, S., Lévesque, M., Plaisier, F., Shmuel, A., Cauli, B., and Hamel, E. (2011). Pyramidal neurons are "neurogenic hubs" in the neurovascular coupling response to whisker stimulation. J. Neurosci. *31*, 9836–9847.

Li, W.L., Fraser, J.L., Yu, S.P., Zhu, J., Jiang, Y.J., and Wei, L. (2011). The role of VEGF/VEGFR2 signaling in peripheral stimulation-induced cerebral neurovascular regeneration after ischemic stroke in mice. Exp. Brain Res. *214*, 503–513.

Lind, B.L., Brazhe, A.R., Jessen, S.B., Tan, F.C., and Lauritzen, M.J. (2013). Rapid stimulus-evoked astrocyte Ca2+ elevations and hemodynamic responses in mouse somatosensory cortex in vivo. Proc. Natl. Acad. Sci. USA *110*, E4678–E4687.

Mangin, J.M., Li, P., Scafidi, J., and Gallo, V. (2012). Experience-dependent regulation of NG2 progenitors in the developing barrel cortex. Nat. Neurosci. *15*, 1192–1194.

McCasland, J.S., and Woolsey, T.A. (1988). High-resolution 2-deoxyglucose mapping of functional cortical columns in mouse barrel cortex. J. Comp. Neurol. *278*, 555–569.

Meng, S., Costa, Lda.F., Geyer, S.H., Viana, M.P., Reiter, C., Müller, G.B., and Weninger, W.J. (2008). Three-dimensional description and mathematical characterization of the parasellar internal carotid artery in human infants. J. Anat. *212*, 636–644.

Molofsky, A.V., Krencik, R., Ullian, E.M., Tsai, H.H., Deneen, B., Richardson, W.D., Barres, B.A., and Rowitch, D.H. (2012). Astrocytes and disease: a neurodevelopmental perspective. Genes Dev. *26*, 891–907.

Munzenmaier, D.H., and Harder, D.R. (2000). Cerebral microvascular endothelial cell tube formation: role of astrocytic epoxyeicosatrienoic acid release. Am. J. Physiol. Heart Circ. Physiol. *278*, H1163–H1167.

Narboux-Nême, N., Evrard, A., Ferezou, I., Erzurumlu, R.S., Kaeser, P.S., Lainé, J., Rossier, J., Ropert, N., Südhof, T.C., and Gaspar, P. (2012). Neurotransmitter release at the thalamocortical synapse instructs barrel formation but not axon patterning in the somatosensory cortex. J. Neurosci. *32*, 6183–6196.

Palàgyi, K., and Kuba, A. (1998). A 3D 6-subiteration thinning algorithm for extracting medial lines. Pattern Recognit. Lett. *19*, 613–627.

Potente, M., Fisslthaler, B., Busse, R., and Fleming, I. (2003). 11,12-Epoxyeicosatrienoic acid-induced inhibition of FOXO factors promotes endothelial proliferation by down-regulating p27Kip1. J. Biol. Chem. *278*, 29619–29625.

Pozzi, A., Macias-Perez, I., Abair, T., Wei, S., Su, Y., Zent, R., Falck, J.R., and Capdevila, J.H. (2005). Characterization of 5,6- and 8,9-epoxyeicosatrienoic acids (5,6- and 8,9-EET) as potent in vivo angiogenic lipids. J. Biol. Chem. *280*, 27138–27146.

Rafelski, S.M., Viana, M.P., Zhang, Y., Chan, Y.H., Thorn, K.S., Yam, P., Fung, J.C., Li, H., Costa, Lda.F., and Marshall, W.F. (2012). Mitochondrial network size scaling in budding yeast. Science *338*, 822–824.

Reddihough, D.S., and Collins, K.J. (2003). The epidemiology and causes of cerebral palsy. Aust. J. Physiother. *49*, 7–12.

Riddle, D.R., Gutierrez, G., Zheng, D., White, L.E., Richards, A., and Purves, D. (1993). Differential metabolic and electrical activity in the somatic sensory cortex of juvenile and adult rats. J. Neurosci. *13*, 4193–4213.

Salic, A., and Mitchison, T.J. (2008). A chemical method for fast and sensitive detection of DNA synthesis in vivo. Proc. Natl. Acad. Sci. USA *105*, 2415–2420.

Shapiro, L.G., and Stockman, G.C. (2001). Computer Vision. (New Jersey: Prentice Hall).

Travençolo, B.A., Martínez Debat, C., Beletti, M.E., Sotelo Silveira, J.R., Ehrlich, R., and Costa, Lda.F. (2007). A new method for quantifying three-dimensional interactions between biological structures. J. Anat. *210*, 221–231.

Tsuji, M., Ohshima, M., Taguchi, A., Kasahara, Y., Ikeda, T., and Matsuyama, T. (2013). A novel reproducible model of neonatal stroke in mice: comparison with a hypoxia-ischemia model. Exp. Neurol. *247*, 218–225.

Vexler, Z.S., Sharp, F.R., Feuerstein, G.Z., Ashwal, S., Thoresen, M., Yager, J.Y., and Ferriero, D.M. (2006). Translational stroke research in the developing brain. Pediatr. Neurol. *34*, 459–463.

Viana, M.P., Tanck, E., Beletti, M.E., and Costa, Lda.F. (2009). Modularity and robustness of bone networks. Mol. Biosyst. *5*, 255–261.

Wang, Y., Okamoto, M., Schmitz, F., Hofmann, K., and Südhof, T.C. (1997). Rim is a putative Rab3 effector in regulating synaptic-vesicle fusion. Nature *388*, 593–598.

Whitaker, V.R., Cui, L., Miller, S., Yu, S.P., and Wei, L. (2007). Whisker stimulation enhances angiogenesis in the barrel cortex following focal ischemia in mice. J. Cereb. Blood Flow Metab. *27*, 57–68.

Whiteus, C., Freitas, C., and Grutzendler, J. (2014). Perturbed neural activity disrupts cerebral angiogenesis during a postnatal critical period. Nature *505*, 407–411.

Woolsey, T.A. (1978). Some anatomical bases of cortical somatotopic organization. Brain Behav. Evol. *15*, 325–371.

Woolsey, T.A., and Wann, J.R. (1976). Areal changes in mouse cortical barrels following vibrissal damage at different postnatal ages. J. Comp. Neurol. *170*, 53–66.

Zeng, C., Pan, F., Jones, L.A., Lim, M.M., Griffin, E.A., Sheline, Y.I., Mintun, M.A., Holtzman, D.M., and Mach, R.H. (2010). Evaluation of 5-ethynyl-2′-deoxyuridine staining as a sensitive and reliable method for studying cell proliferation in the adult nervous system. Brain Res. *1319*, 21–32.

Zhang, C., and Harder, D.R. (2002). Cerebral capillary endothelial cell mitogenesis and morphogenesis induced by astrocytic epoxyeicosatrienoic Acid. Stroke *33*, 2957–2964.

Zlokovic, B.V. (2010). Neurodegeneration and the neurovascular unit. Nat. Med. *16*, 1370–1371.